Bridging the gap between atomic microstructure and electronic properties of alloys: The case of (In,Ga)N

J. A. Chan, J. Z. Liu, and Alex Zunger[*]

National Renewable Energy Laboratory, Golden, Colorado 80401, USA

(Received 26 March 2010; revised manuscript received 12 May 2010; published 15 July 2010)

The atomic microstructure of alloys is rarely perfectly random, instead exhibiting differently shaped precipitates, clusters, zigzag chains, etc. While it is expected that such microstructural features will affect the electronic structures (carrier localization and band gaps), theoretical studies have, until now, been restricted to investigate either perfectly random or artificial "guessed" microstructural features. In this paper, we simulate the alloy microstructures in thermodynamic equilibrium using the static Monte Carlo method and study their electronic structures explicitly using a pseudopotential supercell approach. In this way, we can bridge atomic microstructures with their electronic properties. We derive the atomic microstructures of InGaN using (i) density-functional theory total energies of $\sim$50 ordered structures to construct a (ii) multibody cluster expansion, including strain effects to which we have applied (iii) static Monte Carlo simulations of systems consisting of over 27000 atoms to determine the equilibrium atomic microstructures. We study two types of alloy thermodynamic behavior: (a) under lattice incoherent conditions, the formation enthalpies are positive and thus the alloy system phase-separates below the miscibility-gap temperature T_{MG}, (b) under lattice coherent conditions, the formation enthalpies can be negative and thus the alloy system exhibits ordering tendency. The microstructure is analyzed in terms of structural motifs (e.g., zigzag chains and $In_nGa_{4-n}N$ tetrahedral clusters). The corresponding electronic structure, calculated with the empirical pseudopotentials method, is analyzed in terms of band-edge energies and wave-function localization. We find that the disordered alloys have no electronic localization but significant hole localization, while below the miscibility gap under the incoherent conditions, In-rich precipitates lead to strong electron and hole localization and a reduction in the band gap.

I. INTRODUCTION

Substitutional $A_xB_{1-x}C$ alloys made of semiconductor or insulator components AC and BC are used extensively in numerous optoelectronic applications because they offer desirable electronic properties that are normally not attainable by pure AC and BC.[1,2] The atomic microstructure of alloys is rarely perfectly random, instead exhibiting differently shaped precipitates, clusters, zigzag chains, and manifesting some degree of short-range order (SRO) and sometimes long-range order (LRO).[2] While it is expected that such microstructural features will affect the electronic structures, including carrier localization[3–11] and band gaps,[8,12–15] theoretical studies have, until now, been restricted to investigate either perfectly random alloys (SRO=0; LRO=0) (Refs. 16–18) or "guessed," nonrandom microstructural features.[8,13,14,16,17,19–23] Atomic-scale spatial inhomogeneities in otherwise random alloys can lead to carrier localization and modified optical properties, which possess a controlling effect on the material properties.[1,2] Here we obtain *ab initio* atomic microstructures of a prototype isovalent semiconductor alloy [zinc-blende (ZB) GaN-InN] using cluster expansions based on density-functional theory (DFT) calculations followed by Monte Carlo simulations. We emphasize the occurrence of various atomic microstructures, such as nanoscale precipitates, tetrahedral clusters, and In-N-In-… zigzag chains. Using large supercell pseudopotential theory, we then calculate the corresponding electronic properties, emphasizing the degree of spatial wave-function localization of the band-edge states and change in the band gaps. We find how the electronic structures track the atomic-scale microstructures, thus estab-

lishing a bridge between atomic-scale structures and electronic properties in alloys.

We consider two thermodynamic situations: lattice-incoherent alloy thermodynamics and lattice-coherent alloy thermodynamics.[24] The terms "coherence" and "incoherence" we refer to are *not* with respect to the substrate (as in epitaxy) but with respect to the alloy matrix, e.g., a coherent precipitate having continuous crystal planes across the phase boundary between it and the film matrix whereas an incoherent precipitate having the dislocations, grain boundaries, and so on to disengage it from the film matrix.

A. Lattice-incoherent alloy thermodynamics

Under lattice-incoherent thermodynamics, the crystal lattices of the different phases/precipitates are disengaged from each other by, for example, dislocations, grain boundaries, and so on. For a typical semiconductor alloy, the energy of an alloy configuration $E(A_xB_{1-x}C)$ is usually higher than the energies of the equivalent amount of constituents $xE(AC) + (1-x)E(BC)$, *each at its own lattice constant*, a_{AC} and a_{BC}. The excess alloy enthalpy $\Delta H = E(A_xB_{1-x}C) - [xE(AC) + (1-x)E(BC)]$ is thus positive. Consequently, the semiconductor alloy thermodynamics is characterized by a "miscibility-gap" temperature, T_{MG}, in the composition (x)-temperature (T) phase diagram, below which the alloy phase-separates into AC-rich and BC-rich solid solutions. Incoherent microstructure thus exhibits nanoscale precipitates and clusters (i.e., AC-rich or BC-rich disordered solid solution phases) below the miscibility temperature, leading to strong deviations of the electronic structure from that of the

random alloy, at low growth temperatures. The existence of lattice incoherence with its attended $\Delta H > 0$ is usually taken as a theoretical explanation for the observed In-rich clusters inside InGaN samples in the transmission electron microscope (TEM) measurement.[7] However, recent atom-probe experimental results dispute the formation of the In-rich clusters and attribute the observed In cluster to the electron beam damage in TEM.[25]

B. Lattice-coherent alloy thermodynamics

Under lattice-coherent thermodynamics, all the phases assume a single-crystal lattice. Since often the energy $E(A_xB_{1-x}C)$ is *lower* than the energy of the *strained constituents* $xE(AC,a) + (1-x)E(BC,a)$, then the excess alloy enthalpy ΔH is reduced relative to the incoherent case and can be negative. The phase separation (into AC-rich and BC-rich solid solutions) expected in the incoherent case is hindered in the coherent case. The alloy system would even exhibit ordering tendency below a critical temperature T_C.[24,26] In the case of InGaN alloys, the ground-state structures and the phase diagrams for the coherent and incoherent cases have been previously calculated in Ref. 24. The phase diagrams show that the disordered solid solution phase of the coherent alloy is stabilized, as evidenced by the phase transition temperature being reduced from $T_{MG} = 1870$ K (the miscibility gap in the incoherent case) to $T_C = 600$ K in the coherent case. In terms of long-range ordering, phase-separation is predicted for the incoherent case, whereas ordering (e.g. the formation of a chalcopyrite phase) is predicted for the coherent case. However, to the authors' knowledge, the formation of coherence-induced order structures have not been reported experimentally. This might be due to the high dislocation density present in grown InGaN samples leading to alloy incoherence.[7] (Note: in this paper we discuss only strain-induced ordering,[2,24] not surface-induced ordering).

II. COMPUTATIONAL METHOD

The methods for obtaining and characterizing the atomic microstructures and electronic structures are described diagrammatically in Fig. 1. We next describe each step separately.

A. Calculation of the alloy atomic microstructure

We determine the formation enthalpies of the bulk-coherent and bulk-incoherent InN-GaN zinc-blende systems using the cluster-expansion (CE) approach based on the first-principles local-density approximation (LDA) calculations.[24,26,27] Using the obtained cluster expansion as an energy functional, we perform static Monte Carlo (MC) simulations to determine the atomic microstructures in thermodynamic equilibrium at some typical indium concentration x and temperature T. The atomic lattice configurations obtained from the MC simulations are then relaxed to the minimum strain energy using valence force-field (VFF) model. To characterize the obtained alloy atomic microstructures, Warren-Cowley SRO parameters are calculated. The detailed analysis on some specific atomic microstructures
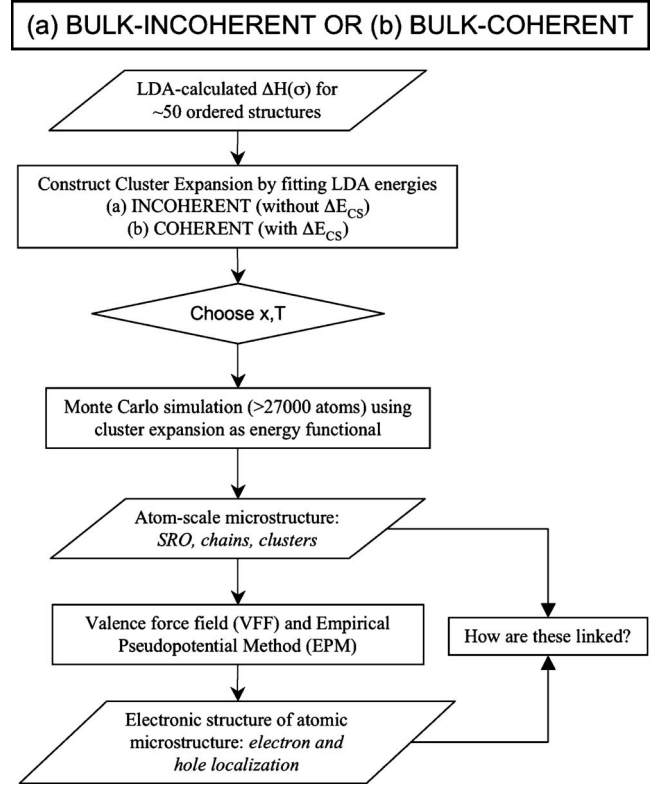

FIG. 1. Flowchart describing how atomic-scale configurations are generated in (a) incoherent or (b) coherent alloy cases and how the corresponding electronic structure is calculated.

such as In-N-In… zigzag chains, tetrahedral clusters, and precipitates will be provided as well.

1. Cluster expansion

In a mixed-basis CE (MBCE),[27] the formation energy $\Delta E(\sigma)$ of a structure, $\sigma = s_0, s_1, \ldots, s_N$ (i.e., a specific atomic occupation on each lattice) consisting of N numbers of atoms, can be expressed in terms of pair and many-body interactions,

$$\Delta E_{CE}(\sigma) = J_0 + \frac{1}{N}\left[\sum_i J_i s_i + \sum_{i,j} J_{ij} s_i s_j + \sum_{i,j,k} J_{ijk} s_i s_j s_k + \cdots\right]$$

$$+ \sum_k \frac{\Delta E_{CS}(\hat{\mathbf{k}},x)}{4x(1-x)}|S_\sigma(k)|^2 e^{-(|k|/k_c)^2}, \quad (1)$$

where s_i is the pseudospin variable ($s_i = -1$ or $s_i = 1$ if site i is occupied by atom type A or B, respectively), the $J_{ij}, J_{ijk}, \ldots$ terms are the interaction energies of pair, three-body, etc., figures. The last term in Eq. (1) is used to describe the atomic-size mismatch effects in which $S_\sigma(k)$ is the Fourier transform of the pseudospin variables of configuration σ, $\Delta E_{CS}(\hat{\mathbf{k}},x)$ is defined as the strain energy of long period superlattice $(AC)_m/(BC)_n$ $[n/(m+n)=x$ and $m, n \to \infty]$ along crystal direction $\hat{\mathbf{k}}$, and the exponential term is an attenuation function for short-concentration wave.[28,29]

All the quantities that define the MBCE in Eq. (1) are determined by *ab initio* total-energy calculations. The inter-
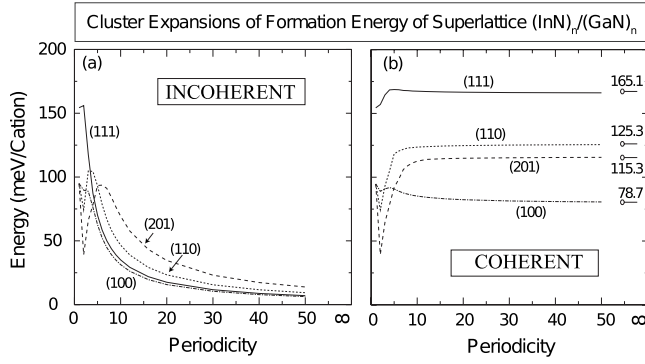
FIG. 2. $(InN)_p/(GaN)_p$ superlattice energies vs periodicity for (a) incoherent and (b) coherent cases. In (a) the energy for longer periods asymptotically tends to zero.

action energies $\{J_{ij},\ldots\}$ are obtained by fitting of $\Delta E_{\rm CE}(\sigma)$ to a set of *ab initio* calculated formation energies $\{\Delta E_{\rm LDA}(\sigma)\}$. We use two separate cluster expansions to describe the two types of alloy thermodynamic behaviors: (a) in a *bulk-incoherent* alloy, each phase maintains its own lattice structures and lattice constants, thus being disengaged from its surrounding alloy matrix. The lattice coherent strain energy is zero and we have used a cluster expansion without the constituent strain term [i.e., without the last term in Eq. (1)]. To illustrate this behavior, Fig. 2(a) shows the $(InN)_p/(GaN)_p$ superlattice formation enthalpy vs the periodicity, p, of the superlattice for different layer orientations. We see that asymptotically all values go to zero for the incoherent case since the asymptotic energies represent the fully disengaged InN and GaN.

(b) In the *bulk-coherent* alloy, each subphase maintains its lattice coherence with the $A_xB_{1-x}C$ alloy matrix. This cluster expansion is constructed *with* the constituent strain term [i.e., the last term in Eq. (1)]. Figure 2(b) shows the formation enthalpy of the superlattice $(InN)_p/(GaN)_p$ vs the periodicity, p, in which the asymptotic finite values for different superlattice orientation represent the coherence lattice strain energies.

The two cluster expansions are fitted to total energies of a set of selected ordered structures calculated with the LDA (Ref. 30) and projected augmented wave method, as implemented in the VASP code.[31,32] The Brillouin zone is sampled with Monkhost-Pack k-point meshes with roughly constant mesh densities corresponding to $9 \times 9 \times 9$ for the fcc unit cell. The plane-wave basis set cutoff energy is set as 435 eV. The error bounds on ΔE is about 1 meV/atom. A "leave-many-out" cross-validation (CV) score is adopted as a fitting quality parameter.[33] The interactions are obtained by first eliminating several ordered structures from the fit and choosing the interactions that results in the best prediction error (i.e., the CV score) for the eliminated configurations. The process is repeated, including more LDA input structures at each step, until a desired accuracy is achieved.[24]

2. Monte Carlo simulations of the atomic microstructures

In this paper, the MC simulations are performed using the EMC2 code included in the ATAT software package.[34,35] We use an ordinary METROPOLIS Monte Carlo (not kinetic Monte Carlo) where the cation types are swapped between cation sites. Whether the swap is accepted, or rejected, is decided by the probability, $e^{-\Delta E/k_B T}$, where ΔE is the energy difference between the atomic configurations before and after the swap, as determined by the cluster expansion functional. Like in any METROPOLIS MC, the entropy is treated by the statistical repetition of this procedure. The simulations are performed using the canonical ensemble. A sufficiently large simulation cell is used to ensure there is no restriction to the development of the alloy atomistic microstructures. A supercell consisting of >27000 irreducible atoms is found to converge the first pair SRO parameters (described later in Sec. IV) within 0.0002.

We take ten snapshots from each MC simulation to represent the alloy microstructures at given x, T. The electronic properties of three of these snapshots are calculated: the snapshot with the highest number of In-N-In chains (with length of two In atoms), the snapshot with the lowest number of In-N-In chains and the snapshot with the number of In-N-In chains closest to the average out of the ten snapshots. In this way, we can confirm that the trends in the results are not affected by variations in atomic configurations at the particular x, T.

The random solid solution microstructure is obtained by running the MC simulations at the very high temperature of $T = 10000$ K (for all these structures, the magnitude of the SRO parameters is determined to be less than 0.06, where SRO=0 for a perfect random configuration). For the coherent and incoherent thermodynamic situations, we consider temperatures ranging from room temperature to the typical sample growth temperature in experiments, $T = 300 - 1000$ K. We focus our studies to the region of In concentration below $x < 50\%$ (i.e., $x = 0 - 20$ %) since previous findings suggest that high exciton localization occurs at such low concentrations.[7,16]

3. Relaxation of the atomic microstructures

The atomic configurations (i.e., the particular atomic distributions on ideal lattice sites) in thermodynamic equilibrium are obtained via the MC simulation. However, in order to obtain a detailed real-space description of the *relaxed atomic positions* starting from the MC configuration, we allow local atomic relaxation by using the VFF approach[36–38] using parameters from Ref. 39. (Note: the *energies* used in MC do include relaxation effects since the cluster expansion uses the *ab initio* energies of geometry-relaxed structures as direct input). The lattice parameters for these supercell structures are relaxed under the constraint of cubic symmetry in order to mimic the thermodynamic limit.

4. Characterization of alloy atomic microstructures from the Monte Carlo simulations

Warren-Cowley SRO parameters $a_l(x)$ used to statistically describe the microstructures are defined as,

$$\alpha_l(x) = 1 - \frac{P(l)}{x}, \tag{2}$$

where $P(l)$ is the probability of finding an indium atom being the lth nearest neighbor of an gallium atom in a given

TABLE I. Calculated and experimental GaN-InN VBM offsets.

Method	Zinc blende	Wurtzite
LDA-LAPW[a]	0.26	0.48
LDA[b]	1.11	-
HSE06[c]	-	0.62
Experiment[d]	-	0.58

[a]Reference 44.
[b]Reference 45.
[c]Reference 18.
[d]Reference 46.

$In_xGa_{1-x}N$ atomic microstructure. The character of the alloy microstructure can be classified by the sign of the SRO parameter: $\alpha_l > 0$ corresponds to an association of "like" atoms (i.e., "clustering"), and $\alpha_l < 0$ corresponds to an association of "unlike" atoms (i.e., "anticlustering"), while $\alpha_l = 0$ means the alloy is perfectly random.

The SRO provides a statistical means to measure the atomic microstructures in the MC simulation samples.[40] SRO, however, describes neither the structural fluctuations nor the structural details. Previous studies have investigated the effect of tetrahedral clusters $N[A_nB_{4-n}]$ (Ref. 41) and the isolated In-N-In zigzag chains on the hole localization.[16,17,22] In this paper, we relate the electronic structures to these two types of atomic motifs inside our MC samples, i.e., the number of In-N-In chains with different lengths and the number of the tetrahedral clusters $N[In_nGa_{4-n}]$ with $n = 1-4$.

B. Calculation of electronic structure of Monte Carlo generated alloy configurations

1. Empirical pseudopotential calculations

We use the empirical pseudopotential method (EPM) rather than LDA to calculate electronic structures so as to correct the systematic errors underlying LDA regarding the band gap.[42] We adjust the screened pseudopotential to reproduce the experimentally measured band gaps at Γ, X, and L, the effective masses, pressure coefficients, biaxial strain deformation potential, and band offsets. The general procedure is described in Ref. 42. The current zinc-blende GaN-InN pseudopotential was correlated with respect to our previous one[43] by fixing the InN band gap to 0.76 eV. As before, it is fitted to effective masses, pressure coefficients, and GW-calculated high-symmetry band energies.[43] While fitting the pseudopotential of two materials their relative band offset needs to be fitted as well to assure correct positioning of the energy levels. The fit is simply decided by the $G = 0$ component of the screened pseudopotential. In what follows we explain which target value of the offset we aim to fit. The value of the unstrained valence-band offset $\Delta E_V^{(ZB)}(GaN/InN)$ is controversial[18,44,45] (see Table I). We know that the wurtzite (WZ) offset is larger than the ZB offset (see the linearized augmented planewave (LAPW) calculation of Ref. 44). The most recent WZ offset calculation using a hybrid DFT functional (HSE06) (Ref. 18) is 0.62 eV,

in good agreement with the recent experimental value[46]) of 0.58 eV. Thus, the ZB offset must be $\Delta E_V^{(ZB)} < 0.62$ eV [the recent deformation-potential-corrected LDA value of $\Delta E_V^{(ZB)} = 1.1$ eV for ZB (Ref. 45) is in contradiction with this]. We use the same ZB offset from previous work, 0.26 eV.[43] A higher offset, in between 0.3–0.6 eV, combined with linear bowing (supported by hybrid/screen exchange calculations[16,17]) leaves the valence-band maximum (VBM) values at low In concentration ($x \leq 20\%$) unchanged.

For a given atomic configuration, the EPM calculations are run with the folded spectrum method with no spin-orbit coupling.[47] The calculation is run until convergence of the eigenvalues is reached within a tolerance of 10^{-6} eV. The VBM, conduction-band minimum (CBM), and electronic wave functions are direct outputs.

2. Quantifying degrees of carrier localization

A robust and intuitive method to measure the carrier localization of a given wave-function is to use the number of cations on which a significant amount of the wave-function is spatially distributed. We first define the charge contribution from state j per cation at lattice site i by integrating the wave-function modulo squared within a volume, V,

$$Q_i = \int_V |\Psi_j|^2 dV, \tag{3}$$

where $V = (a)^3/4$, and a is the lattice constant of alloy, and Q_i is normalized so that the sum over N cations $\Sigma_0^N Q_i = 1$. Next, we count the number of cations (NC) with the highest Q_i values in the material that holds 80% (arbitrary choice) of the charge. The *percentage volume* is defined as the ratio of NC over the total number of cations, in the supercell. For a fully delocalized wave-function, the percentage volume is 80% and for the fully localized wave-function, the percentage volume tends to 0%. We can then show the real-space spatial distribution of the wave function by highlighting all the NC cations within the supercell. In contrast, depicting the spatial distribution of wave functions using isosurfaces can be misleading.

III. RESULTS: ATOMIC MICROSTRUCTURES OF InGaN

A. Incoherent alloy atomic-scale structure: Formation of precipitates

Many authors have implicitly assumed the incoherent scenario and created some microstructure that is supposed to reflect it. Examples of such assumed structures include the random alloy,[16–18] 100% pure quantum-dotlike clusters embedded in a pure GaN matrix,[8,13,19,20] an isolated In atom in GaN,[21] and isolated In-N-In chains.[16,17,22] We have calculated the incoherent CE and the MC calculations are carried out to simulate the more realistic microstructure that occur in incoherent conditions. Under such conditions, calculations show that the excess enthalpies of (ordered or random) alloys are *positive*, and correspondingly, the phase diagram [Fig. 3(a)] shows a miscibility line ($T_{MG} = 1870$ K at $x = 43\%$), below which the alloy phase-separates into *AC*-rich plus *BC*-rich alloys.
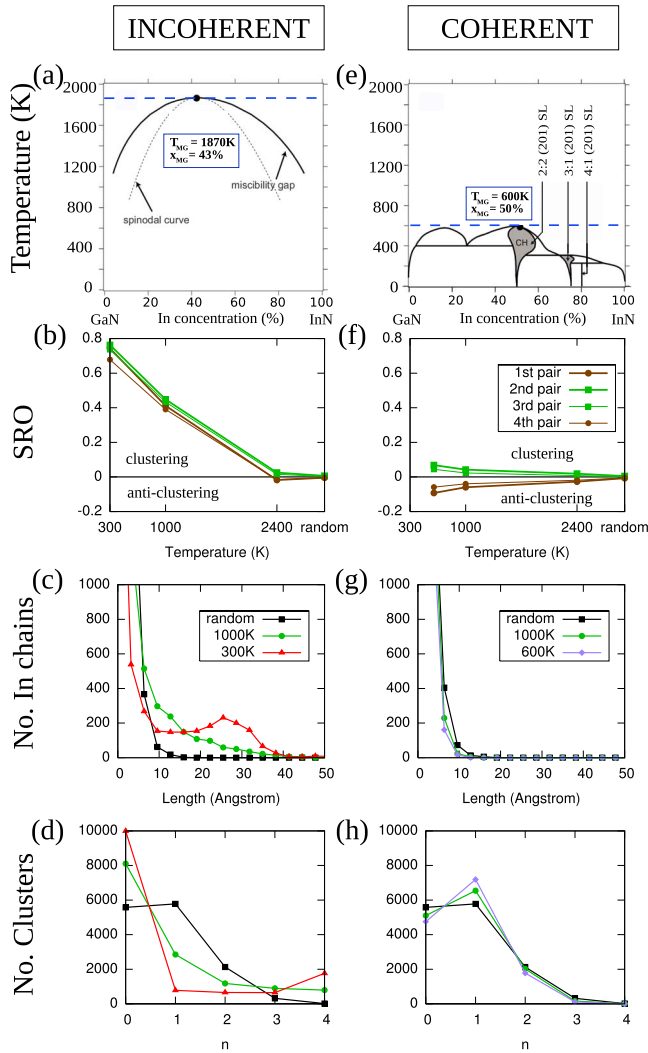
FIG. 3. (Color online) Thermodynamic and structural properties of InGaN zinc-blende alloy under the incoherent and coherent thermodynamic situations. [(a) and (e)] Calculated composition-temperature phase diagram. Detailed structural analysis of MC snapshots at $x=20\%$: [(b) and (f)] the short-range order parameters, [(c) and (g)] number In-N-In chains, and [(d) and (h)] number of $N(In_nGa_{4-n})$ tetrahedral clusters.

1. Short-range order

The short-range order parameters [Fig. 3(b)] of the first up to fourth nearest neighbors at alloy composition $x=20\%$ are all positive at low T ($T \le 1000$ K) indicating clustering. At high $T > 1000$ K, the disordered solid solution phase is thermodynamically stable. In this case, the first- and the fourth-nearest-neighbor SRO are negative, indicating anticlustering tendency, whereas the second- and third-nearest-neighbor SRO parameters are positive, as has been predicted previously.[26,28] In zinc-blende tetrahedral semiconductor alloys with lattice mismatched AC and BC, the (201) superlattice structure turns out to be most capable of relaxing the strain energy.[26] Therefore, the SRO of the disordered solution phase $In_xGa_{1-x}N$, above the miscibility gap, shows the anticlustering tendency in first and fourth nearest neighbors and clustering tendency in the second and third nearest neighbors.

2. Zigzag chains

Figure 3(c) shows the number of In-N-In zigzag chains as a function of chain length for samples at varying temperatures with $x=20\%$. For the random alloy, the probability of finding a chain drops off quickly with the increasing length (squares). For the incoherent alloy at $T=1000$ K (circles) and $T=300$ K (triangles), the probability of finding longer In-N-In chains is much higher with respect to random statistics. The difference is even more significant at $T=300$ K.

3. Tetrahedral clusters

Figure 3(d) shows the number of N-centered tetrahedral clusters, i.e., $N(In_nGa_{4-n})$ in the alloy microstructure at $x=20\%$. For the random alloy, the number of clusters follows the predictions of the Bernoulli random alloy model,[41] where for In concentrations up to $x=20\%$, there are no $N(In_4)$ clusters, and thus no pure InN regions. At finite temperature, the incoherent alloys at $x=20\%$ have fewer $N(In_1Ga_3)$ and $N(In_2Ga_2)$ clusters but more $N(Ga_4)$ and $N(In_4)$ clusters compared to the random alloy, indicating a significant clustering tendency[41] and formation of pure InN regions.

The spatial distribution of the chains with different lengths [3.1 Å (2 In, gray), 9.6 Å (4 In, black), 15.9 Å (6 In, cyan), and 22.3 Å (8 In, red)] and clusters [In_1 (gray), In_2 (black), In_3 (cyan), and In_4 (red)] are shown in Figs. 4(a)–4(d) and 5(a)–5(d) for In concentrations $x=1\%$ and $x=20\%$, respectively. Precipitates are predicted in the incoherent alloys at $T=300$ K at $x=1\%$ as well as $T=1000−300$ K at $x=20\%$. This is consistent with the phase diagram [Fig. 3(a)]. At $x=20\%$ [Figs. 5(c) and 5(d)], the interface between the precipitate and the alloy matrix is interdiffused at $T=1000$ K while the precipitate at $T=300$ K has a much sharper boundary. In addition, the precipitate at $T=1000$ K is spherical in shape while the formation at $T=300$ K is an ellipsoid. This may be due to the different interface energies along different crystal orientations.

B. Coherent alloy atomic-scale structure above T_C: similar to the random alloy

Due to the lattice coherence strain energy, the InGaN alloy has been converted from a phase-separating system to an ordering system, which is manifested in the composition-temperature phase diagram [Fig. 3(e)]. Two observations of the phase diagram can be noted. First, the phase transition temperature is significantly suppressed from $T_{MG}=1870$ K in the incoherent case to $T_C=600$ K. Second, there is a chalcopyrite ordering at $x=50\%$. In terms of this ordered structure, we are not aware of any published experiments. This may be due to the high density of dislocations and grain boundaries in the normal grown InGaN alloy samples that relax the lattice coherent constraint. Here we only study the microstructures of the disordered solid solutions above the coherent T_{MG} [Fig. 3(e)].

1. Short-range order

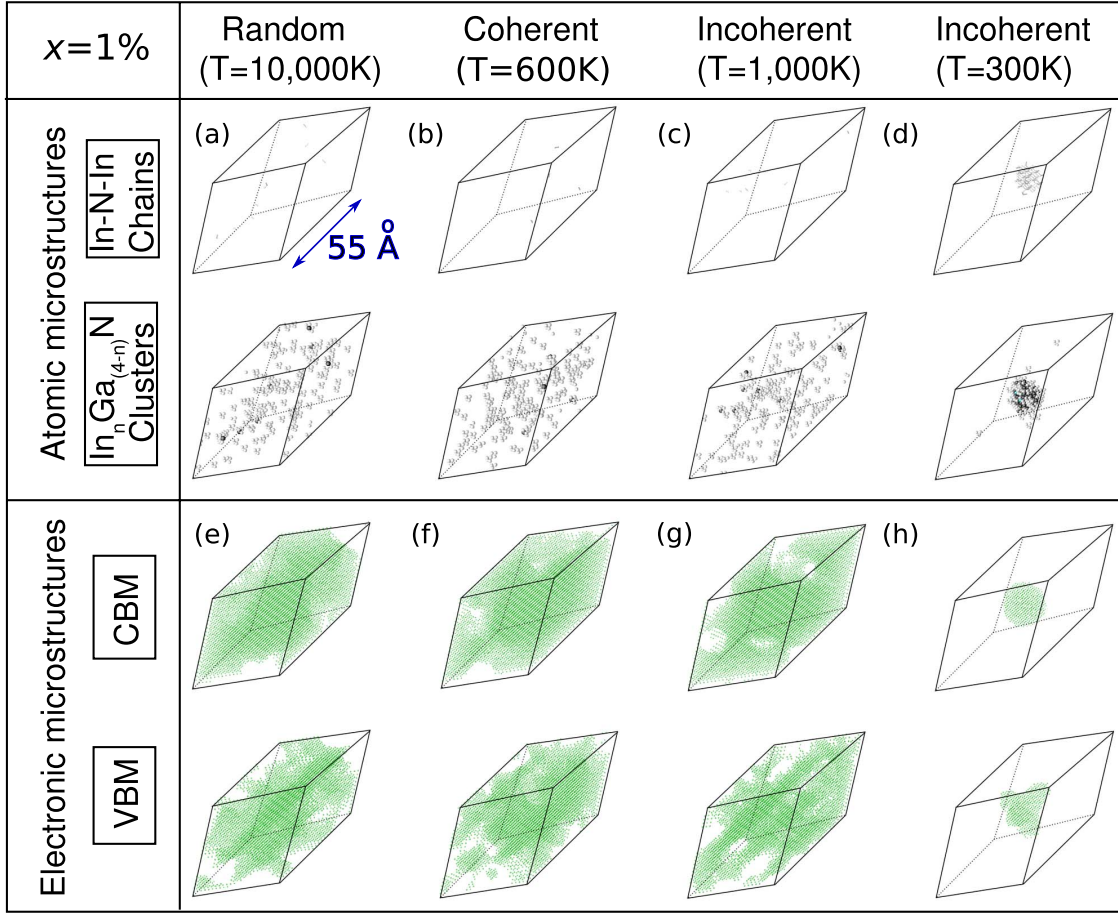The SRO parameters for the first- and the fourth-nearest-neighbor pairs, calculated for the MC samples at $x=20\%$

FIG. 4. (Color online) Atomic configurations and electronic structures of a typical Monte Carlo snapshot of InGaN zinc-blende alloy at $x=1\%$: (a) random alloy, (b) coherent alloy at $T=600$ K, (c) incoherent alloy at $T=1000$ K, and (d) incoherent alloy at $T=300$ K. (a)–(d) show In-N-In chains [3.1 Å (2 In, gray), 9.6 Å (4 In, black), 15.9 Å (6 In, cyan), and 22.3 Å (8 In, red)], and N-centered $[N(In_nGa_{4-n})]$ tetrahedral clusters, $[In_1$ (gray), In_2 (black), In_3 (cyan), and In_4 (red)]. (e)–(h) highlight all the cations that hold 80% of the CBM, or VBM, charge density.

[Fig. 3(f)], are negative, whereas the second and the third SRO parameters are positive. The disordered solid solution phases therefore exhibit anticlustering tendency. Since disordered solution phases at relatively high temperature ($T=2400$ K) are inherently lattice coherent (i.e., only one phase in the system), the SRO parameters calculated for both the incoherent alloy and the coherent alloy are very close. In the coherent alloy, the anticlustering SRO parameters are more pronounced than those in the incoherent alloy because of the suppressed phase transition temperature.

2. Zigzag chains

The number In-N-In chains are very similar to the random alloy [Fig. 3(g)], though there are significantly fewer chains of length of less than 10 Å in comparison with the random alloys. This is consistent to the more pronounced anticlustering SRO tendency.

3. Tetrahedral clusters

Figure 3(h) shows that the number of $N(Ga_4)$ clusters is slightly reduced and the $N(In_1Ga_3)$ tetrahedral clusters is in-

creased at $T=1000$ K and $T=600$ K, which is consistent with the anticlustering tendency of the coherent alloy. The numbers of $N(In_3Ga_1)$ and $N(In_4)$ tetrahedra remain small, showing that local In concentrations above 50% is a rare occurrence when $x \le 20\%$.

The atomic microstructures of the coherent alloys in real space [Fig. 4(b) for $x=1\%$ and Fig. 5(b) for $x=20\%$] do not show significant deviation from those of the random alloy: the chains and clusters are homogeneously distributed.

IV. RESULTS: ELECTRONIC STRUCTURE AND CARRIER LOCALIZATION OF THE CALCULATED MICROSTRUCTURES

We consider the electronic structure of both 1% In-dilute [Figs. 4(e)–4(h)] and 20% In-concentrated [Figs. 5(e)–5(h)] alloys. The degree of localization of electrons (CBM) and holes (VBM) is depicted in these panels by highlighting those cations (NC) that carry 80% of the wave-function in the respective CBM and VBM states (see Sec. II). The charge density of the top three levels of the valence band are
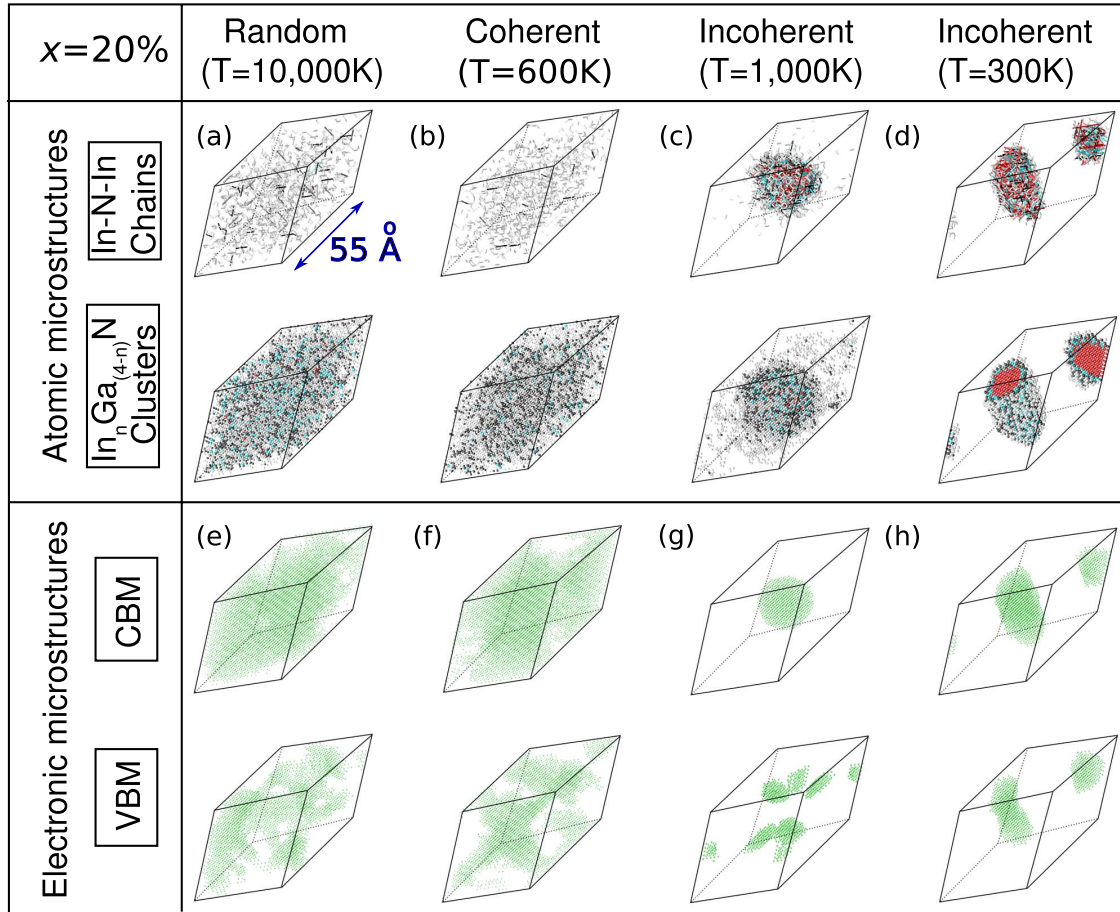
FIG. 5. (Color online) Atomic configurations and electronic structures of a typical Monte Carlo snapshot of InGaN zinc-blende alloy at $x=20\%$: (a) random alloy, (b) bulk-coherent alloy at $T=600$ K, (c) bulk-incoherent alloy at $T=1000$ K, and (d) bulk-incoherent alloy at $T=300$ K. (a)–(d) show In-N-In chains [3.1 Å (2 In, gray), 9.6 Å (4 In, black), 15.9 Å (6 In, cyan), and 22.3 Å (8 In, red)], and N-centered [$N(In_nGa_{4-n})$] tetrahedral clusters, [In_1 (gray), In_2 (black), In_3 (cyan), and In_4 (red)]. (e)–(h) highlight all the cations that hold 80% of the CBM, or VBM, charge density.

summed together to calculate the hole localization at the VBM. Figures 6(a)–6(c) uses the *percentage volume* in the whole system of >27000 atoms to quantify the hole and electron localization with respect to In concentration.

A. Electron and hole localization

1. Random alloys

Assuming random statistics is the simplest and most popular way to describe alloys. For the electron, we find that 80% of the charge density is located on about 75% of the total volume of the system, meaning that the electrons are essentially delocalized [top panel of Fig. 6(a) (squares)]. Spatially, the electrons are seen to be homogeneously distributed over the whole system at $x=1\%$ [Fig. 4(e)] and at $x=20\%$ [Fig. 5(e)]. In contrast, the holes in the VBM are significantly localized, as seen in the bottom panel of Fig. 6(a) (squares), where the localization is most significant in the range of In concentrations $x=10-20$ %. Comparison of the electronic structure and alloy microstructures can be made by examining Figs. 4(a) and 4(e) for $x=1\%$, and Figs. 5(a) and 5(e) for $x=20\%$. There is no obvious correlation

between the In-N-In chains and the CBM or VBM localization. This is in contrast to previous studies,[16,17,22] which show clear, strong localization originating from *isolated* In-N-In chains.

We also show how converged system size is important in order to obtain correct results for localization. Figure 6(a) shows the hole localization of the random alloy, calculated using 64 irreducible atoms (crosses), 512 atoms (empty circles), and over 27,000 atoms (squares). For the supercell with over 27,000 atoms, 80% of the VBM is located on just 20–30% of the total volume for concentrations $x=10-20$ %, indicating significant localization. However, for the 512 atom supercell, this value becomes 60–70%, and further changes to 70–80% for the 64 atom cell, indicating very weak localization. In the latter case, even the trend of the hole localization vs concentration is not well predicted. The calculation of a large number of atoms is important to include structural fluctuations not included in a smaller supercell. This shows that localization calculated using smaller sized supercells (e.g., 32 atom[16], 64 atom[17], 72 atom[22] supercells) may give different results regarding localization. However, we note that VBM and CBM energies remain unaffected by system size.
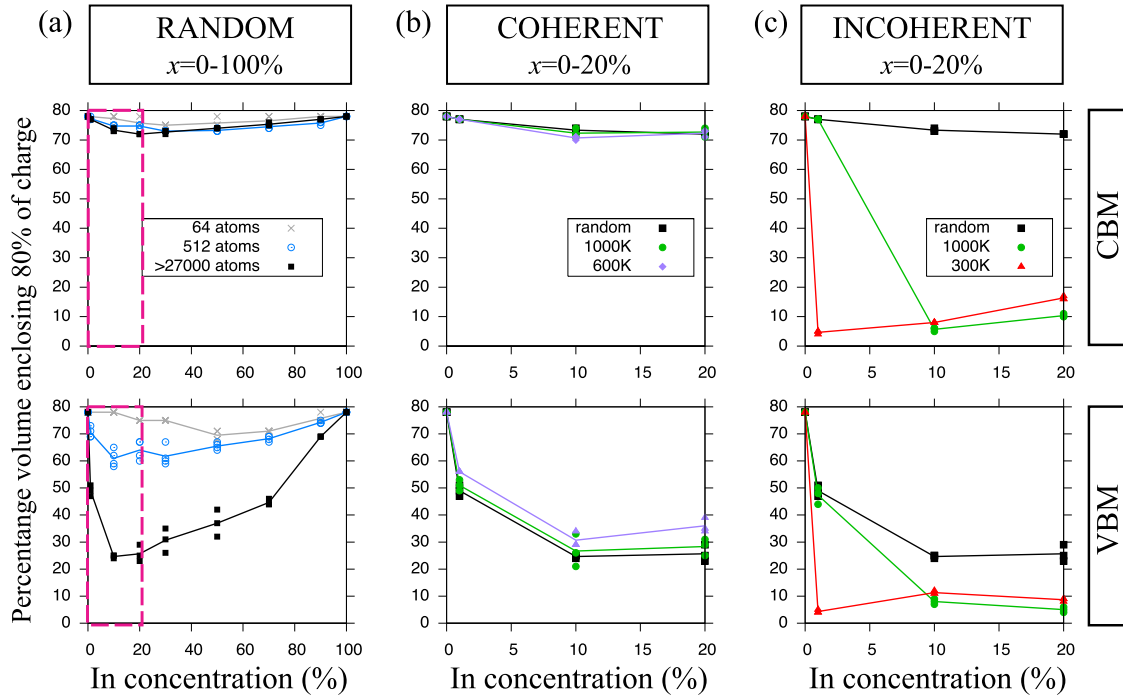
FIG. 6. (Color online) The percentage volume with 80% of the VBM (CBM) charge density for the (a) random, (b) bulk-coherent, and (c) bulk-incoherent alloys. Results are calculated for the three separate Monte Carlo snapshots at each concentration and temperature. In (a) the effects of the supercell size on the electron and hole localization are present as well.

2. Coherent alloys

Figure 6(b) shows that for the coherent alloy, there is no significant difference between the percentage volume of VBM and CBM states of the disordered solid solution phases at $T=1000$ K and $T=600$ K and those of the random alloys. The degree of localization [Fig. 6(b)] shows that while electron localization is unchanged by temperature, the hole localization decreases only slightly as temperature decreases. There is greater (although still small) range of data points for $T=1000$ K (circles) due to more configurational fluctuation at this temperature. The distribution of hole and electron states in real space are shown in Figs. 4(f) and 5(f).

Overall we can conclude that the SRO in the disordered solid solutions does not lead to a significant deviation in the electronic and hole localization from that of random alloys. Since only the hole is localized, exciton localization seems unlikely unless the electron binds with a hole localized in the VBM.

3. Incoherent alloys

The most dramatic deviation from randomness of electronic structure is demonstrated by the formation of precipitates in the incoherent alloy. The percentage volume in Fig. 6(c) quantifies the hole and electron localization, showing that 80% of the CBM and VBM charges is located on only 5–20 % of the total volume. Figures 4(g), 4(h), 5(g), and 5(h) show how the electrons and holes are not distributed homogeneously but tracks the alloy precipitates. Analysis of Q_i values show the highest values for electrons are at the center of the precipitate, whereas the VBM charge tends to

localize on atoms surrounding the precipitate, as was noted for artificially constructed In quantum-dot calculations.[8]

B. Factors contributing to localization: Chemical effect versus size-mismatch effect

The isovalent semiconductor alloy InGaN has two constituents (i.e., In and Ga) with very similar chemical properties. It is thus not easy to understand the strong hole localization in terms of the chemical differences of two alloying components. As shown in GaAsN and GaAsP alloys, the significant chemical differences (e.g., the electronegativity) between the substituting atoms As/N and P/N lead to a drastic carrier localization.[48] In order to separate the chemical vs lattice effects on the localization, we compare the electronic properties of the relaxed structures with those of the unrelaxed structures where all bond lengths are instead constrained to the ideal Ga-N bond lengths (Fig. 7).

For random alloys, the CBM charge is unaffected [percentage volume: 72% (relaxed) vs 76% (ideal)] while the VBM changes significantly [percentage volume: 25% (relaxed) vs 77% (ideal)]. Note: we expect similar results for coherent alloys. This behavior suggests that *random fluctuations in the alloy leads to hole localization due to local lattice distortions*.

For incoherent alloys with a precipitate, the CBM is unaffected by atomic relaxation [percentage volume: 10% (relaxed) vs 11% (ideal)]. The electron localization appears to be due to chemical effects of the In clusters [percentage volume: 10% for the sample with precipitates vs 72% for the random alloy sample]. The hole localization, however, is strongly affected by atomic relaxation [6% (relaxed) vs 51%
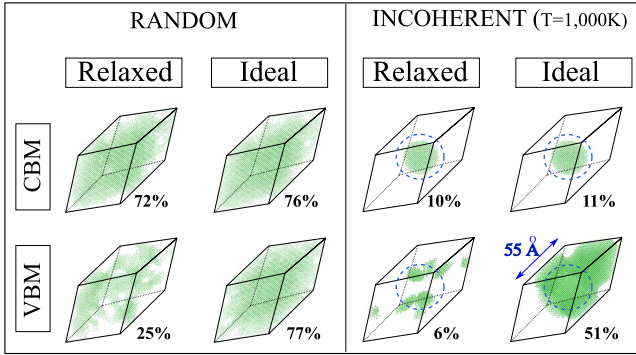
FIG. 7. (Color online) Comparison between VBM (CBM) localization of relaxed vs ideal (GaN) atomic coordinates for the random and incoherent alloys at $T = 1000$ K at $x = 20\%$. Cations that hold 80% of the VBM (CBM) charge density are highlighted in green.

(ideal)]. The flower-shaped charge density of the VBM is not present when the atomic coordinates are not relaxed.

The lattice distortion due to the InN-GaN size-mismatch (11%) explains why InGaN has such a pronounced hole localization effect, compared to alloys such as InGaAs (Ref. 21) with 7% mismatch. The localization predicted for isolated In-N-In chains[16,17,22] may also be understood in terms of the lattice distortion caused by the chain.

C. CBM and VBM energies

1. Coherent alloys

The VBM and CBM energies for the random alloy are shown in Fig. 8(a). Figure 8(b) shows that, compared to the random alloy, there is negligible change in the CBM energies for the coherent alloy up to $x = 20\%$ at temperatures above 600 K. The largest calculated change from the random alloy is in the VBM energy at $x = 20\%$, $T = 600$ K and is of a value

of only 26 meV lower than the random alloy VBM energy. To put this value in perspective, the error in the VBM energy (as determined by comparing the values calculated from the three MC snapshots described in Sec. II) is found to be about 8 meV. This shows that the anticlustering SRO of the coherent alloy has the effect of lowering the VBM but the effect is practically negligible for the temperatures and concentration ranges studied in this paper.

2. Incoherent alloys

The CBM and VBM energies vs In concentration are shown in Fig. 8(c). At $x = 1\%$ and $T = 1000$ K, the alloy exhibits disordered solid solution phases, there is no obvious deviations of the CBM and VBM of the random alloy. The alloys have the In-rich precipitates embedded in a GaN rich solid solution phase in other cases (Figs. 4 and 5). The corresponding VBM and CBM undergo a significant change, whereby the VBM shifts up and the CBM shifts down. As a consequence, the band gap is dramatically reduced, for example, the band gap is reduced to 1.25 eV at 300 K compared to the gap of 2.52 eV of the random alloys. This trend is similar to the behavior of pure InN clusters in pure GaN.[8,19,21] It is interesting to note that the band gap associated with the In-rich precipitate (with pure InN center) is significantly larger than that of a pure InN constituent. This could be due to the size confinement of the precipitates within the alloy matrix.

V. DISCUSSION: RELATING ELECTRONIC STRUCTURE TO ATOMIC MICROSTRUCTURE

Our main conclusions for the case of the InGaN zinc-blende alloy are : (i) the structural fluctuations in the random alloy readily lead to significant hole localization; (ii) the anticlustering SRO in the disordered solid solution phases (the incoherent alloy above miscibility gap and the coherent alloy
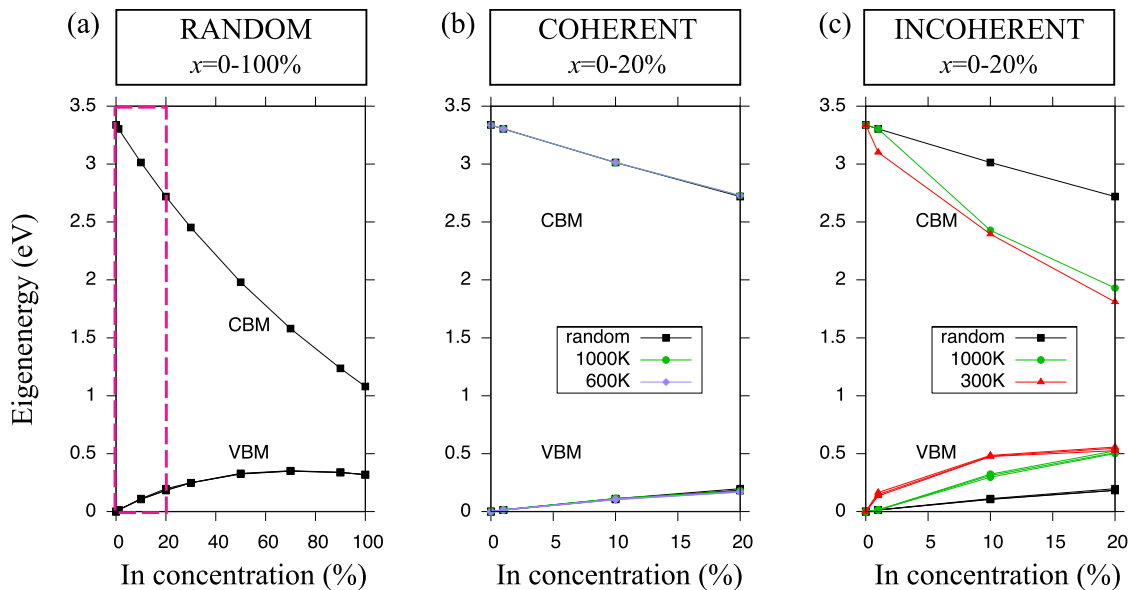

FIG. 8. (Color online) The conduction band minimum (CBM) and the top three valence band maximum (VBM) states of InGaN zinc-blende (a) random ($x = 0 - 100$ %), (b) coherent ($x = 0 - 20$ %), and (c) incoherent ($x = 0 - 20$ %) alloys.

above 600 K) slightly reduces the hole localization in comparison with the random alloy; (iii) the presence of the In-rich precipitates (incoherent alloys below the miscibility gap) results in strong electron and hole localization and strongly reduces the band gap relative to the random alloys; and (iv) the lattice distortion of the atomic microstructures due to the size mismatch between the In and Ga atoms is crucial to understand the strong hole localization in the InGaN alloy.

In light of the structural similarity and thermodynamic similarity (e.g., similar miscibility gap temperature) in zinc-blende and wurtzite InGaN alloys, we believe our conclusions on the ZB alloy are also applicable to the WZ alloy. In experiments, the internal quantum efficiency of WZ-InGaN light-emitting diode is very high in spite of the high dislocation density in the alloy samples grown by molecular beam epitaxy and metal-organic chemical-vapor deposition methods (e.g., 10^9–10^{10} cm^{-2}). It was proposed that the exciton localization due to the In-rich precipitates prevents the diffusion of excitons toward the nonirradiative centers.[7] However, recent atom-probe experiments from Galtrey *et al.*[49] showed that the alloy film is composition homogeneous without the reported In rich clusters in the TEM observations.[7] Our results may provide a clue to understand this controversy. The structural fluctuation inside the random alloys can provide comparable hole localization in comparison to the In-rich precipitates. It is worth noting that the predicted peak of hole localization at $x \sim 10$–20 % [Fig. 6(a)] agrees with the highest light emission efficiency measured in experiments very well.[7]

VI. SUMMARY

In summary, we employ the *ab initio* computational method, the cluster expansion approach, and static Monte Carlo simulations to study the realistic atomic microstructures of InGaN zinc-blende alloy at varying thermodynamic conditions, in contrast to the widely adopted random alloy model and the artificially "guessed" structures. The empirical pseudopotential method is used to study the electronic properties of the obtained atomic microstructures including the electron and hole localization, CBM and VBM energy, and the band gap. The correlations between the atomic microstructures in thermodynamic equilibrium and the corresponding electronic properties are established. We find that the structural fluctuations in the random and disordered alloys can lead to strong hole localization. The anticlustering tendency in the disordered solid solutions (in both the incoherent and coherent situations but more significant in the coherent case) slightly reduces the hole localization in comparison to the random alloy. The presence of the In-rich precipitates (the LRO in the incoherent situation below miscibility gap) leads to a drastic localization of both electrons and holes and a significantly reduced band gap.

*alex.zunger@nrel.gov

[1] A.-B. Chen and A. Sher, *Semiconductor Alloys: Physics and Material Engineering* (Plenum, New York, 1995).

[2] A. Zunger and S. Mahajan, *Atomic Ordering and Phase Separation in III-V Alloys in Handbook of Semiconductors*, 2nd ed. (Elsevier, Amsterdam, 1994), Vol. 3.

[3] S. Permogorov and A. Reznitsky, J. Lumin. **52**, 201 (1992).

[4] E. Lifshitz, I. Dag, I. Litvin, G. Hodes, S. Gorer, R. Reisfeld, M. Zelner, and H. Minti, Chem. Phys. Lett. **288**, 188 (1998).

[5] B. Shklovskiĭ and A. L. Éfros, Sov. Phys. JETP **33**, 468 (1971).

[6] B. Shklovskiĭ and A. L. Éfros, Sov. Phys. Semicond. **14**, 487 (1980).

[7] S. F. Chichibu *et al.*, Nature Mater. **5**, 810 (2006).

[8] P. R. C. Kent and A. Zunger, Appl. Phys. Lett. **79**, 1977 (2001).

[9] F. A. Ponce, S. Srinivasan, A. Bell, L. Geng, R. Liu, M. Stevens, J. Cai, H. Omiya, H. Marui, and S. Tanaka, Phys. Status Solidi B **240**, 273 (2003).

[10] D. M. Graham, A. Soltani-Vala, P. Dawson, M. J. Godfrey, T. M. Smeeton, J. S. Barnard, M. J. Kappers, C. J. Humphreys, and E. J. Thrush, J. Appl. Phys. **97**, 103508 (2005).

[11] T. Miyanaga, T. Azuhata, S. Matsuda, Y. Ishikawa, S. Sasaki, T. Uruga, H. Tanida, S. F. Chichibu, and T. Sota, Phys. Rev. B **76**, 035314 (2007).

[12] L. Bellaiche and A. Zunger, Phys. Rev. B **57**, 4425 (1998).

[13] T. Saito and Y. Arakawa, Physica E **15**, 169 (2002).

[14] I. Gorczyca, S. P. Łepkowski, T. Suski, N. E. Christensen, and A. Svane, Phys. Rev. B **80**, 075202 (2009).

[15] L. K. Teles, J. Furthmüller, L. M. R. Scolfaro, J. R. Leite, and F. Bechstedt, Phys. Rev. B **63**, 085204 (2001).

[16] B. Lee and L. W. Wang, J. Appl. Phys. **100**, 093717 (2006).

[17] X. Wu, E. J. Walter, A. M. Rappe, R. Car, and A. Selloni, Phys. Rev. B **80**, 115201 (2009).

[18] P. G. Moses and C. G. V. de Walle, Appl. Phys. Lett. **96**, 021908 (2010).

[19] L.-W. Wang, Phys. Rev. B **63**, 245107 (2001).

[20] S. Chen, J. Nanosci. Nanotechnol. **9**, 1226 (2009).

[21] L. Bellaiche, T. Mattila, L.-W. Wang, S.-H. Wei, and A. Zunger, Appl. Phys. Lett. **74**, 1842 (1999).

[22] Q. Liu, J. Lu, Z. Gao, L. Lai, R. Qin, H. Li, J. Zhou, and G. Li, Phys. Status Solidi B **247**, 109 (2010).

[23] K. A. Mäder and A. Zunger, Phys. Rev. B **51**, 10462 (1995).

[24] J. Z. Liu and A. Zunger, Phys. Rev. B **77**, 205201 (2008).

[25] T. M. Smeeton, M. J. Kappers, J. S. Barnard, M. E. Vickers, and C. J. Humphreys, Appl. Phys. Lett. **83**, 5419 (2003).

[26] J. Z. Liu, G. Trimarchi, and A. Zunger, Phys. Rev. Lett. **99**, 145501 (2007).

[27] D. B. Laks, L. G. Ferreira, S. Froyen, and A. Zunger, Phys. Rev. B **46**, 12587 (1992).

[28] C. Wolverton, V. Ozoliņš, and A. Zunger, J. Phys.: Condens. Matter **12**, 2749 (2000).

[29] L. G. Ferreira, V. Ozoliņš, and A. Zunger, Phys. Rev. B **60**, 1687 (1999).

[30] J. P. Perdew and A. Zunger, Phys. Rev. B **23**, 5048 (1981).

[31] G. Kresse and J. Furthmüller, Comput. Mater. Sci. **6**, 15 (1996).

[32] G. Kresse and J. Furthmüller, *VASP the Guide* (Universität Wien, Wien, Austria, 2007).

[33] The cross-validation score is calculated as the average prediction error for a given number of ordered structures by the cluster expansion that is least-squares fitted from the rest of configurations in a data pool.

[34] A. van de Walle and M. Asta, Modell. Simul. Mater. Sci. Eng. **10**, 521 (2002).

[35] A. van de Walle ATAT software package at http://www.its.caltech.edu/~avdw/atat/

[36] K. Kim, P. R. C. Kent, A. Zunger, and C. B. Geller, Phys. Rev. B **66**, 045208 (2002).

[37] P. N. Keating, Phys. Rev. **145**, 637 (1966).

[38] R. M. Martin, Phys. Rev. B **1**, 4005 (1970).

[39] K. Kim, W. R. L. Lambrecht, and B. Segall, Phys. Rev. B **53**, 16310 (1996).

[40] In its strict definition, SRO does not apply for a mixture of two phases. For convenience, we just extend its application to demonstrate the clustering LRO.

[41] S.-H. Wei, L. G. Ferreira, and A. Zunger, Phys. Rev. B **41**, 8240 (1990).

[42] H. Fu and A. Zunger, Phys. Rev. B **55**, 1642 (1997).

[43] P. Piquini and A. Zunger (unpublished).

[44] S.-H. Wei and A. Zunger, Appl. Phys. Lett. **69**, 2719 (1996).

[45] Y.-H. Li, A. Walsh, S. Chen, W.-J. Yin, J.-H. Yang, J. Li, J. L. F. D. Silva, X. G. Gong, and S.-H. Wei, Appl. Phys. Lett. **94**, 212109 (2009).

[46] P. D. C. King, T. D. Veal, C. E. Kendrick, L. R. Bailey, S. M. Durbin, and C. F. McConville, Phys. Rev. B **78**, 033308 (2008).

[47] L.-W. Wang and A. Zunger, J. Chem. Phys. **100**, 2394 (1994).

[48] L.-W. Wang, L. Bellaiche, S.-H. Wei, and A. Zunger, Phys. Rev. Lett. **80**, 4725 (1998).

[49] M. J. Galtrey, R. A. Oliver, M. J. Kappers, C. J. Humphreys, D. J. Stokes, P. H. Clifton, and A. Cerezo, Appl. Phys. Lett. **90**, 061903 (2007).